

Lawrence Berkeley National Laboratory

LBL Publications

Title

Design study for a compact, two-stage, laser-plasma-based source of positron beams

Permalink

<https://escholarship.org/uc/item/2995k7b9>

Journal

Plasma Physics and Controlled Fusion, 65(8)

ISSN

0741-3335

Authors

Amorim, Lígia D
Benedetti, Carlo
Bulanov, Stepan S
[et al.](#)

Publication Date

2023-08-01

DOI

10.1088/1361-6587/ace3f1

Peer reviewed

Design study for a compact, two-stage, laser-plasma-based source of positron beams

Lígia D. Amorim, Carlo Benedetti, Stepan S. Bulanov,
Davide Terzani, Axel Huebl, Carl B. Schroeder, Jean-Luc
Vay, Eric Esarey

Lawrence Berkeley National Laboratory, Berkeley, CA, USA

E-mail: sbulanov@lbl.gov

18 July 2023

Abstract.

Owing to their large accelerating gradients, plasma-based accelerators have attracted considerable interest as potential drivers for future, compact electron-positron colliders. Despite great progress achieved in plasma-based electron acceleration, positron acceleration still remains a challenging task, with an efficient positron source being the prerequisite for such acceleration. Here a concept for a compact, two-stage plasma-based positron source is discussed. In the first stage the positrons are created by a multi-GeV electron beam produced by a laser-plasma accelerator interacting with a solid density foil. In the second stage the positrons are captured and accelerated in a plasma wave driven by either an electron beam or a laser pulse. Three potential configurations of such a source are considered: (i) A single electron beam is used for both the creation of positrons in the foil and for driving the wakefield in the second stage; (ii) A train of two electron beams is used: the positrons produced by the trailing beam in the foil are captured and accelerated in the second stage by the plasma wave generated by the leading beam; and (iii) A single electron beam is used to produce positrons in the foil and an independent laser pulse is coupled to the second stage to drive the plasma wave. These three configurations show different degrees of effectiveness with positron capture efficiency, varying from less than a percent to almost half of all produced positrons.

Keywords: plasma, wakefield, accelerator, positron, laser, Geant4, particle-in-cell

Submitted to: *Plasma Phys. Control. Fusion*

1. Introduction

Particle colliders are unique tools for advancing fundamental and high-energy physics research at the energy and luminosity frontiers worldwide [1]. Plasma-based accelerators [2, 3] can sustain accelerating gradients of tens to hundreds of GeV/m, which are several orders of magnitude higher than those produced in standard Radio-Frequency cavities, making them promising candidates as drivers for future compact colliders [4–7].

While high-energy [8], high-efficiency [9], and low-energy-spread [10] plasma-based electron acceleration was demonstrated experimentally, high-quality positron acceleration is significantly more challenging. So far, positron acceleration in a self-driven nonlinear plasma wakefield [11] and in a hollow plasma channel [12] has been demonstrated experimentally, but with a beam quality lower than what has been achieved for electrons. Moreover, one of the main challenges of plasma based positron acceleration lies in efficient creation, capture, and acceleration of high-quality (i.e., with high-charge and energy, and with low emittance and energy spread) positron beams in compact structures, i.e., a compact plasma-based positron source.

In conventional accelerators positrons are usually produced via collisions of high energy electrons or photons with solid density high-Z foils (see, e.g., proposed [13–15] and operational [11] designs), accumulated in a damping ring, and then transported into the accelerator. Compact, plasma-based accelerators, however, present a set of unique requirements for accelerating positron beams efficiently [16]. The most challenging ones are achieving a low energy spread and divergence, as well as the short duration of the beam so the positrons can be efficiently captured in the plasma wakefield. Some progress on overcoming these challenges has recently been achieved [17–28] (see also [29] and references cited therein). Experiments [30, 31] also demonstrated that the electron beams used for positron production in conventional accelerators can be substituted by electron beams produced in a laser-plasma accelerator (LPA).

In this paper we investigate a compact laser-plasma-based positron source based on a two-stage design, which produces, captures, and accelerates positrons. A schematic of the system is shown in Fig. 1. In the first stage positrons are produced as a result of the interaction of an LPA-generated, multi-

GeV electron beam with a solid density foil. Then the positrons are coupled to the second stage, where they are captured and accelerated by a plasma wave. We consider three configurations: (i) A single electron beam produces the positrons in the foil, then both the initial electron beam and the electron-positron pairs enter the second stage, where the electron beam creates a plasma wave which is able to capture and accelerate a fraction of the positrons. (ii) A train of two LPA-produced electron beams interacts with the foil, producing two positron beams. In the second stage the positrons produced by the trailing electron beam are captured into the accelerating and focusing phase of the wakefield produced by the leading electron beam. (iii) A single LPA-produced electron beam is used to produce positrons in the foil, then these positrons are transported and accelerated into an LPA stage powered by an independent laser pulse. This laser-driven wakefield scheme is shown to be the most efficient out of all three configurations for capturing and accelerating most of the positrons produced.

This paper is organized as follows. In Sec. 2 we discuss the interaction of the electron beam, henceforth

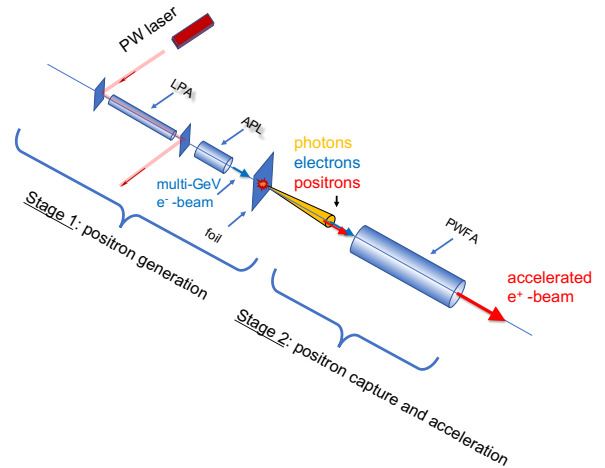


Figure 1. Schematic of the laser-plasma-based positron source. The first stage is constituted by the LPA producing the multi-GeV electron beam, the optics to transport the beam (APL is an active plasma lens [32–34]), and the high-Z foil inside which the electrons emit photons and these photons are converted into electron-positron pairs. The second stage is constituted by a plasma target where the positrons are trapped and accelerated in a plasma wave (in the example depicted the plasma wave is generated by a plasma wakefield accelerator, or PWFA).

called primary beam, with the foil and determine the optimal conditions for positron production and characterize the corresponding quality degradation of the primary beam. In Sec. 3 we investigate the evolution of the primary electron beam and of the electron-positron pairs created by it in the foil (to which we refer to as secondary particles) in the plasma stage where a wakefield is generated by the primary beam alone. In Sec. 4 we explore the second proposed configuration, where a train of two primary electron beams first interact with the foil and is then injected in a plasma together with the secondary particles. The third configuration, where secondary positrons created in the foil by the primary beam are injected and trapped in the wake generated by an independent laser pulse is analyzed in Sec. 5. Conclusions are presented in Sec. 6.

2. Characterization of the secondary particles produced in the interaction of the primary beam with the high-Z foil

In this section we study the process of electron-positron pair production associated with the interaction of the primary electron beam with a solid density foil. The interaction with the foil is modeled with the code GPOS [35] (see also the Appendix for more details), based on the GEANT4 simulation toolkit [36–38].

The primary electron beam, propagating along the z axis, was spatially described by an axis-symmetric bi-Gaussian distribution with RMS sizes $\sigma_{x,p} = \sigma_{y,p} = 0.7 \mu\text{m}$, (transverse) and $\sigma_{z,p} = 0.4 \mu\text{m}$ (longitudinal) at the focal position, an initial energy of 10.1 GeV (the relative RMS energy spread was 0.9%), a RMS divergence $\theta_{x,p} = \theta_{y,p} = 0.3 \text{ mrad}$, and a beam charge of 55 pC (results can be easily rescaled to other values of the charge). The chosen primary electron beam parameters are the ones anticipated for LPA stages driven by current PW-class lasers such as BELLA PW [39]. In the GPOS runs, the primary beam was sampled with 2×10^6 particles to ensure negligible statistical fluctuations. A solid density Tungsten (W) foil of varying thickness was placed at 1.5 mm distance from the primary beam. A virtual particle detector registered the phase space of the particles exiting from the back of the target.

Production of electron-positron pairs takes place in a two-step process. First, photons are produced via bremsstrahlung as the high-energy electrons of the beam are scattered by the target nuclei. The photon spectrum is very broad, with the maximum photon energy extending up to the incident electron energy. Second, electron-positron pairs are produced by the decay near a nucleus of photons with an energy $E_\gamma > 2m_e c^2 = 1.022 \text{ MeV}$ (m_e is the electron mass and

c the speed of light in vacuum). For a target thickness of 1 mm, GPOS simulation results show that out of the electrons and positrons produced that reached the end of the foil, 91 % of the electrons and 100 % of the positrons originated in the decay of the bremsstrahlung photons. The remaining electrons originated from other processes, such as above threshold ionization, Compton scattering, and photoelectric effect. If we compare the final absolute charges of the secondary electron and positron beams with the primary one, then the former is 19 %, while the latter is 17 % of the primary one. The secondary electrons and positrons had axis-symmetric profiles, and the core of both distributions overlapped with that of the primary beam, as can be seen in Fig. 2, where we plot the two-dimensional spatial distribution of the primary beam electrons (green), secondary electrons (blue), and positrons (orange) after the interaction with the foil. The secondary beams lower energy and higher divergence particles fell behind and transversely further away from the primary beam.

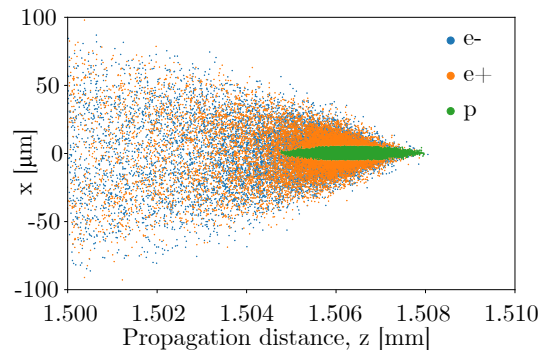


Figure 2. Two-dimensional spatial distribution of the primary beam electrons (p , green), and secondary electrons (e^- , blue) and positrons (e^+ , orange) at the end of the interaction with the 1 mm-long foil.

The energy spectra after the interaction with the foil for primary and secondary particles are shown in Fig. 3. The secondary electrons (blue line) and positrons (orange triangles) are characterized by a monotonically decreasing spectrum with a total of less than 7 % of the charge lying above 3 GeV. Due to the energy loss consequent to each interaction, the primary beam spectra attained a long, low-energy tail (solid green line).

In order to optimize positron production in terms of charge and divergence, and characterize the degradation of the primary beam, we conducted parameter scans varying the primary beam and foil parameters. It was found that the positron and primary electron beams properties after the foil are mainly sensitive to the foil thickness and material, and the primary beam initial mean energy. In particular,

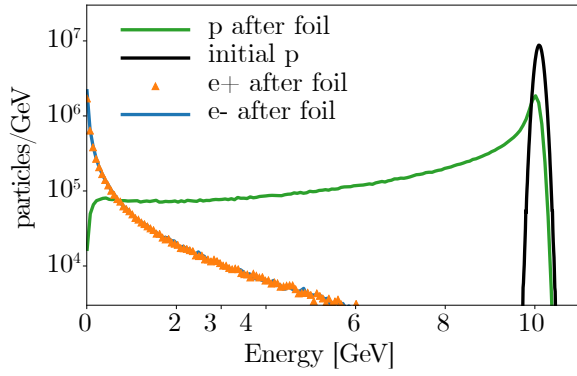


Figure 3. Energy spectra of the primary beam (p) before (black line) and after (green line) the interaction with the 1 mm-long Tungsten foil. Spectra of the secondary electrons (e^- , blue line) and positrons (e^+ , orange triangles) after the interaction.

increasing the foil thickness results in an increase of the produced secondary particles [40]. This is shown in Fig. 4, where we plot (blue line) the positron throughput η_{e^+} , defined as the ratio of the number of positrons that exit the foil over the number of primary electrons that enter it, as function of the foil thickness. This is due to the increase in the number of interactions, which also results in the growth of the primary electrons beam divergence (orange line).

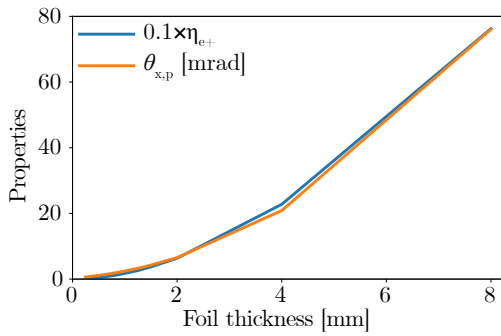


Figure 4. Positron throughput $0.1 \times \eta_{e^+}$ (blue line), defined as the ratio of the number of positrons that exit the foil over the number of primary electrons that enter it, and RMS divergence of the primary beam after the interaction with the foil ($\theta_{x,p}$, orange line) as function of the foil thickness.

Increasing the foil thickness also results in the increase of the divergence of the secondary particles. This is shown in Fig. 5, where we plot the RMS divergence of the secondary electrons (blue and green lines) and positrons (orange and red lines) as a function of the foil thickness for two values of the energy cutoff for particle detection, $E_c = 5$ MeV, and $E_c = 180$ MeV. For small target thicknesses and a cutoff energy of $E_c = 5$ MeV electrons at low energies are, as mentioned before, mostly produced by processes other than pair production. This explains the charge

imbalance between secondary electrons and positrons and the difference in the final RMS divergence that can be seen in the blue and orange lines, respectively. By increasing the energy cutoff for secondary particle detection to $E_c = 180$ MeV, the difference in the final divergence between positrons and electrons is greatly reduced (green and red lines) as most of the high energy electrons are generated in pair with the positrons, which yields a symmetric angular distribution.

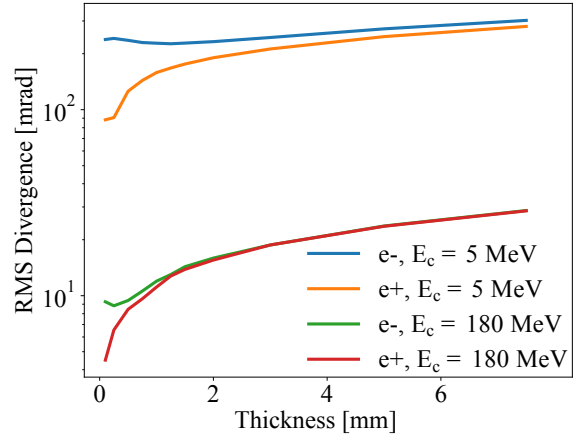


Figure 5. RMS divergence of the secondary electrons and positrons as a function of the foil thickness for different cutoff energies (E_c). For $E_c = 5$ MeV, the difference between the e^- (blue line) and e^+ (orange line) RMS divergence is due to the electrons produced in processes other than pair production (e.g., ionization, Compton scattering, etc.). These contribute to the spectrum at low energies, i.e., high divergence. For a cutoff $E_c = 180$ MeV, the difference in the final divergence between e^- (green line) and e^+ (red line) is greatly reduced.

These results highlight the presence of a trade-off between maximizing the positron beam charge while minimizing the final primary beam and positron beam divergence. The configuration considered in this work used a 1 mm thick Tungsten foil and a primary beam energy of 10.1 GeV to produce enough positrons while keeping the low-divergence required for maximizing the capture of the positrons in the subsequent plasma accelerator stage.

3. Positron source driven by a single LPA-produced electron beam

In this section we examine the positron source realized with a single LPA-produced primary electron beam. Positrons are produced by the primary beam interacting with the foil, then both the primary beam and the secondary electrons and positrons enter the second stage, where the primary beam creates a plasma wave which captures and accelerates a fraction of the positrons.

The positrons parameters are the ones discussed in Sec 2. The plasma stage was modeled with the particle-

in-cell (PIC) code WARPX [41, 42] using the quasi-cylindrical $r - z$ geometry employing one azimuthal mode. The background density in the plasma stage, n_0 , was chosen to match the primary beam length in order to maximize the accelerating wakefields [43], i.e., such that $k_p \sigma_{z,p} = \sqrt{2}$, where k_p is the plasma wavenumber, namely $k_p = (n_0 q_e^2 / \epsilon_0 m_e c^2)^{1/2}$, where q_e is the electron charge, and ϵ_0 the vacuum permittivity. That matching condition corresponds to $n_0 = 3.5 \times 10^{20} \text{ cm}^{-3}$, yielding a plasma wavelength $\lambda_p = 2\pi/k_p = 1.7 \mu\text{m}$. The ratio of the beam density to the ambient plasma density is 0.1, hence we expect the plasma stage to operate, at least initially, in a linear regime. The plasma electron density profile was radially uniform and longitudinally composed by 100 μm linear up and down ramps encompassing a constant density plateau. The background ions were considered immobile. For self-consistent beam space-charge field initialization, the beams were propagated forward ballistically inside WARPX until they reached the end of the foil and an artificial electromagnetic field dumping module (mirror) was used to remove the fields close to the back of the foil. The (r, z) dimensions of the computational domain were $(23.8, 10.3) \mu\text{m}$ (the domain initially contained 84% of the produced positrons), with a longitudinal and transverse resolution of $\Delta z = \sigma_{z,p}/60 = 6.7 \times 10^{-3} \mu\text{m}$ and $\Delta r = \sigma_{x,p}/51 = 1.4 \times 10^{-2} \mu\text{m}$, respectively. The plasma was sampled with 2 particles per cell.

In Fig. 6 we show the lineouts of the longitudinal, E_z , and transverse, $E_r - cB_\phi$, wakefields taken close to the axis of propagation at the beginning of the plasma plateau. The phase region where the wakefield is accelerating and focusing for positrons, hereafter named AFP region (red line in Fig. 6), fell behind the primary beam (green line) and, hence, behind the core of the positron beam (purple line). The few positrons that fall behind the beam right after exiting the foil are too transversely dispersed to be captured by the plasma wave (the characteristic transverse size of the plasma wave is $\sim \lambda_p$). For this reason, after propagating about 0.5 mm, less than 0.03% of the positrons remained within the simulation box. We also note that most of the positrons that remain close to the axis experience defocusing fields (positive part of the orange curve in Fig. 6). As a result, the longitudinal positron beam profile no longer follows that of the electron beam. The transverse evolution (focusing) of the primary beam, occurring over a propagation distance on the order of the betatron wavelength, resulted in the transition of the wakefield structure from the linear into the non-linear regime, further narrowing and also shifting the AFP region making this scheme unsuitable to capture and accelerate positrons efficiently.

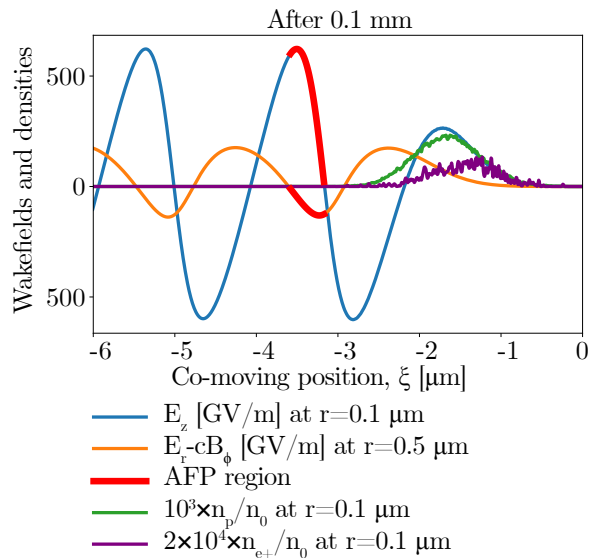


Figure 6. Lineout of the plasma accelerating, E_z (blue); focusing, $E_r - cB_\phi$, (orange) wakefields; primary and positron beams normalized density, n_p/n_0 and n_{e^+}/n_0 ; and the AFP region closest to the beams; plotted along the co-moving variable, $\xi = z - ct$ after the beams reached the plasma plateau. Propagation direction is from left to right side of the plot.

To allow for a higher fraction of the positrons that exit the foil to fall within the AFP phases of the plasma wakefield, a vacuum drift section was introduced between the foil and the plasma stage: by changing the length of the drift, L_{drift} (we considered drift distances of up to 2 mm) it is possible to change the relative delay, T_{delay} , between the secondary positrons and the primary beam, which, ideally, should be equal to the phase distance between the primary electron beam and the AFP region divided by the speed of light. Let us consider a model case of a primary electron beam with relativistic factor γ_1 , and a secondary positron beam with $\gamma_2 < \gamma_1$. Then, considering ballistic motion, we have $L_{drift} \simeq 2\gamma_2^2 c T_{delay} / (1 - \gamma_2^2 / \gamma_1^2)$, assuming $\gamma_1, \gamma_2 \gg 1$. Thus, the higher the energy of the positrons that need to be captured and accelerated, the longer should the vacuum drift be. However, due to the fact that the positrons are produced with broad spectrum the effect of the drift section should be studied in simulations.

The results of simulations with various drift distances showed that the capture of positrons remained well below 1% of the total generated charge. In fact, although the drift allows more of the slower positrons to fall further behind the primary beam, those positrons tend to diverge transversely and are not captured in the wake.

Modeling of the positron source driven by a single electron beam showed that, for a wide range of parameters, less than 1% of positrons is captured and

accelerated. We conclude that a robust and reliable plasma-based high-energy positron source using this configuration is problematic.

4. Positron source driven by a train of two LPA-produced electron beams

In this section we analyze the positron source driven by a train of two LPA-produced primary electron beams. During the interaction with the foil both electron beams produce positrons, then all primary and secondary particles are injected into a plasma stage. While the leading primary beam drives a plasma wave, the positrons from the trailing primary beam are captured and accelerated in it. This configuration is, in principle, similar to the one proposed in Refs. [17, 18], but in our case we assume the two primary beams are produced in a compact LPA setup by using some triggered injection scheme (e.g., laser-induced ionization injection inside a plasma target tailored with two separate high-Z gas sections [44–46]). As an example, in this section we consider two electron beams, one with 10.1 GeV energy and 0.9% energy spread (leading beam), the other with 8.6 GeV energy and 1.1% energy spread (trailing beam). The two beams have the same charge (55 pC) and equal longitudinal and transverse sizes. The longitudinal separation between the beams is 8.8 μm .

After the interaction with the Tungsten foil (modeled, as before, with GPOS, and where we sampled both primary beams with 2×10^6 particles each), primary and secondary beams propagate ballistically in vacuum for 2 mm before entering the plasma stage. The plasma has a density of $n_0 = 1.1 \times 10^{19} \text{ cm}^{-3}$ ($\lambda_p = 10.2 \mu\text{m}$), a length of 1 cm (with 100 μm -long linear entrance and exit ramps), and is transversely uniform.

As before, the plasma stage was modeled with the quasi-cylindrical $r-z$ geometry of WARPX employing one azimuthal mode. The (r, z) dimensions of the computational domain were $(62.9, 13.1) \mu\text{m}$ (the domain initially contained 56% of the produced positrons), with a longitudinal and transverse resolution of $\Delta z = \sigma_{z,p,1}/100 = 4 \times 10^{-3} \mu\text{m}$ and $\Delta r = \sigma_{x,p,1}/130 = 5.4 \times 10^{-3} \mu\text{m}$, respectively. The plasma was sampled with 2 particles per cell. Simulations were run in a Lorentz boosted frame with $\gamma_{\text{boost}} = 2$ with all the output diagnostics in the laboratory frame.

The advantage of this scheme is that, for any given separation between the primary electron beams, by tuning the plasma density it is possible to control the phase in the plasma wave where the positrons generated by the trailing beam will be located and, hence, maximize their capture and acceleration. In the example considered here, the phase of the trailing

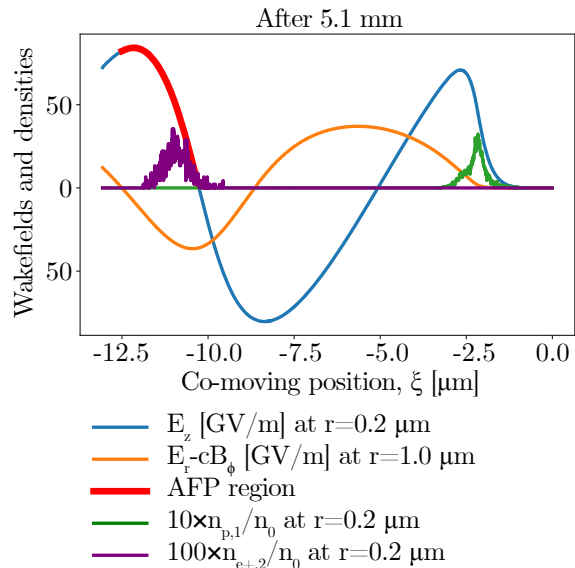


Figure 7. Lineouts of the plasma accelerating, E_z (blue); focusing, $E_r - cB_\phi$, (orange) wakefields; leading primary and trailing positron beams normalized density, $n_{p,1}/n_0$ (green) and $n_{e+,2}/n_0$ (purple) shown as a function of the co-moving variable, $\xi = z - ct$, after the beams propagated 5 mm in the plasma plateau. The AFP region of interest is denoted in red. Propagation direction is from left to right side of the plot.

positrons was such that their core would experience stronger focusing fields, but weaker accelerating fields. This choice enables more charge to be captured. In Fig. 7 we show lineouts of the density of the leading primary beam, $n_{p,1}$ (green line), and that of the trailing positrons, $n_{e+,2}$ (purple line), together with the longitudinal, E_z (blue line), and transverse, $E_r - cB_\phi$ (orange line), wakefields (in red is the AFP region) taken close to the axis of propagation after a 5.1 mm propagation distance. Even though the leading primary beam still performed betatron oscillations (the betatron period of the beam is $\lambda_\beta \approx 1.8 \text{ mm}$), owing to the different density of operation the excited wakefield is more stable than the one in Sec. 3, and the quasi-linear wakefield structure allows the positron beam core to stay within the AFP for the whole acceleration length.

The quasi-linear nature of the wakefield is evident from Fig. 8, where we plot a 2D map of the longitudinal wakefield (red-blue colormap) at the end of the 1 cm-long plasma, as well as the density distribution of the leading primary beam (green) and trailing positron beam (purple). Note that the trailing primary beam and secondary electrons and the leading secondary electrons and positrons were not shown in the plot since they were all quickly defocused or decelerated. This is shown in Fig. 9, where we plot the charge within the AFP region (the radial extent of the AFP region is set by the condition $r < 4 \mu\text{m}$) as a function of the

propagation distance in the plasma for the trailing primary beam (green line), the trailing secondary electrons (blue line), and the trailing positrons (orange line). The initial focusing of the trailing positrons leads to the initial increase in charge. The loss of the lower energy and higher divergence positrons leads to the slow reduction of charge after the first 4 mm of propagation, when the plasma wakefields became stable. The overall capture efficiency of this scheme (defined as the charge in the AFP region at the end of the plasma, 1 pC, divided by the total positron charge generated in the foil, 9 pC) is 11%. We note that recent advanced concepts of beam driven positron acceleration [26, 28], which use transversely tailored plasmas to optimize the acceleration, could, in principle, be employed. However, we do not expect these schemes to provide a significantly different capture efficiency compared to the scheme considered here.

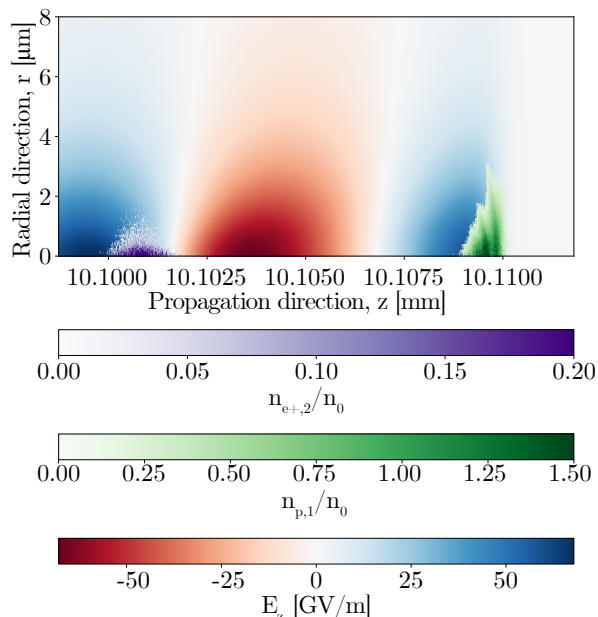


Figure 8. 2D plot of the leading primary (green color-map) and trailing positron (purple) beams densities normalized to the peak plasma background density, overlapping the longitudinal plasma wakefield (red-blue colormap).

As discussed above, the two LPA-produced electron beams configuration is similar to the one proposed in [17, 18]. Despite the lower electron beam energies and total charge used in our simulations, the positron beam production yields similar results. The energy transformation efficiency from the electron beams to the positron beam is 1.3×10^{-4} in [17, 18] and 0.9×10^{-4} in our scheme. In terms of the number of positrons, the efficiencies are 7.5×10^{-3} and 9×10^{-3} , respectively.

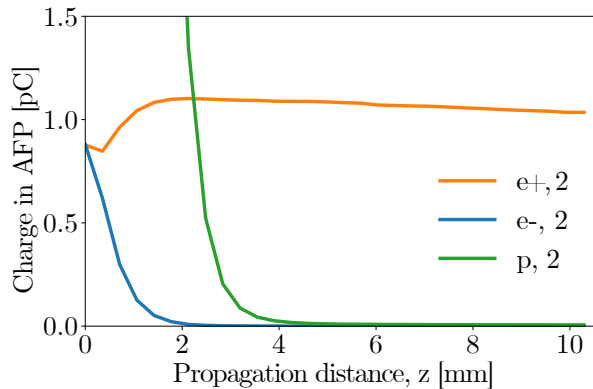


Figure 9. Plots of the trailing primary (green), positron (orange) and secondary electron (blue) charges inside the AFP region ($r < 4 \mu\text{m}$).

5. Positrons from an LPA-produced electron beam trapped and accelerated into an LPA stage driven by an independent laser pulse

In this section we study the positron source that uses an LPA-generated electron beam to create the positrons in a foil, as described in Sec. 2, and capture and accelerate them in a subsequent LPA stage powered by an independent laser driver.

We consider a laser pulse with a duration $\tau_l = 20$ fs (Full-Width-Half-Maximum), a wavelength $\lambda_l = 0.815 \mu\text{m}$, a spot at focus $w_l = 30 \mu\text{m}$ (defined as the radius of $1/e^2$ of the intensity), and a peak field amplitude $E_l = 5.91$ TV/m (resulting in a normalized vector potential amplitude of $a_0 = q_e A_0 / m_e c = 1.5$, where A_0 is the peak laser vector potential), focused on the entrance ramp of a 1 cm-long plasma channel. In order to provide an idealized modeling of the dynamics of the positrons captured by the wakefield generated by the laser pulse, the LPA stage is located right after the solid target. A more realistic description should take into consideration the distance required to in-couple the positrons and the laser driver into the plasma stage. Although we expect the performance of the scheme to depend on the details of the in-coupling, the current study aims at exploring the maximum performance of this scheme. Details on a potential scheme to in-couple the laser and the positrons stage are discussed in Ref. [47]. The longitudinal density profile of the plasma features 100 μm -long linear entrance and exit ramps (the laser is focused in the middle of the entrance ramp) encompassing a plateau with density of $3.55 \times 10^{17} \text{cm}^{-3}$. The transverse profile is parabolic with a matched radius of 30 μm in the plateau region.

Modeling was performed using the azimuthal mode decomposition modality of WARPX, using two modes (this is required to represent the linearly polarized laser). The (r, z) dimensions of the computational

domain were $(112.1, 98.1) \mu\text{m}$ (the domain initially contained 87% of the produced positrons), with a longitudinal and transverse resolution of $\Delta z = \lambda_l/51 = 1.6 \times 10^{-2} \mu\text{m}$ and $\Delta r = w_l/205 = 1.5 \times 10^{-1} \mu\text{m}$, respectively. The plasma was sampled with 4 particles per cell. Simulations were run in a Lorentz boosted frame with $\gamma_{\text{boost}} = 2$ with all the output diagnostics in the laboratory frame.

The delay between the drive laser pulse and the primary electron beam was chosen so that the positrons would remain in the AFP region after propagating through a cm-long plasma. In Fig. 10 we show lineouts of the longitudinal, E_z (blue), and transverse, $E_r - cB_\phi$ (orange), wakefields taken close to the axis of propagation after a propagation distance of 1.7 mm (dotted line) and 9.9 mm (solid line). We also show lineouts of the density of the primary beam, n_p (green line), and that of the trailing positron beam, n_{e+} (purple) after 9.9 mm of propagation. We see that in the first 2.0 mm of propagation the laser excited wakefields compete with that generated by the primary electron beam, leading to irregularities in the wake structure near the positrons (dashed blue line near $\xi \simeq -70 \mu\text{m}$). After that, the primary beam is strongly defocused and the wakefields become regular and stable.

The defocusing of the primary beam as well as the focusing of the positron beam is clear when inspecting the two-dimensional plot in Fig. 11, where the beam densities (green for the primary beam, purple for the positron beam) are shown together with a map of the longitudinal wakefield (red-blue colormap, blue is accelerating for the positrons). The charge of the secondary electrons, which were strongly defocused, dropped to below 0.2% within the AFP region and is not plotted. The peak accelerating and focusing wakefields are, on average, 28.5 GV/m, and -8.1 GV/m, respectively. Those values are weaker than the ones observed in the scenario of Sec. 4, but in this case most of the positrons experience values close to them.

As the positron beam gets focused, its density increases and it begins to flatten (beamload) the accelerating wakefield, as can be seen in Fig. 10 (solid blue under the red lines near $\xi \simeq -70 \mu\text{m}$). This beamloading effect allows more uniform acceleration throughout the beam.

Given the stability of the wakefields, the charge of the positrons in the AFP region varied less than 0.1% after the initial 2 mm. The propagation of the positrons in the LPA stage leads to the formation of a positron bunch, resulting from the loss of low-energy (there are no positrons below 180 MeV at the end of the cm-long plasma) and high-divergence particles, with an energy core between 3.5 GeV and 5 GeV, and with a charge of 4.2 pC, corresponding to a capture

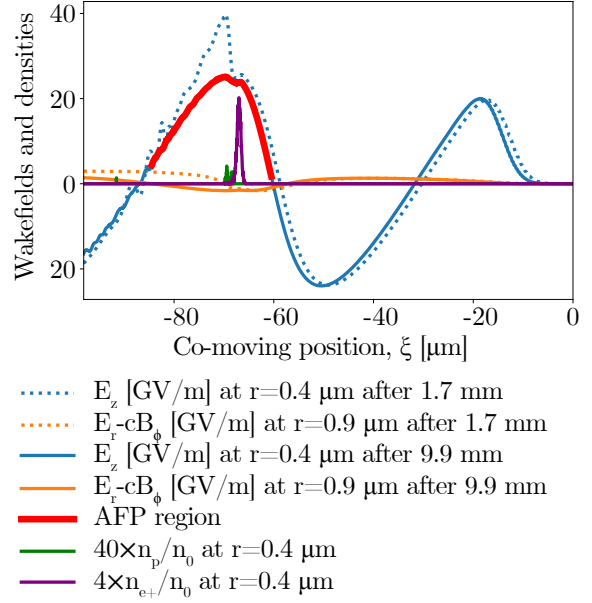


Figure 10. Lineouts of the plasma accelerating, E_z (blue); focusing, $E_r - cB_\phi$, (orange) wakefields; primary and positron beams normalized densities, n_p/n_0 (green) and n_{e+}/n_0 (purple), close to the axis and as a function of the co-moving variable, $\xi = z - ct$. The AFP region of interest is denoted in red. Lineouts were taken after the laser and positrons propagated 1.7 mm (dashed lines) and 9.9 mm (solid line) in the plasma. Propagation direction is from left to right side of the plot.

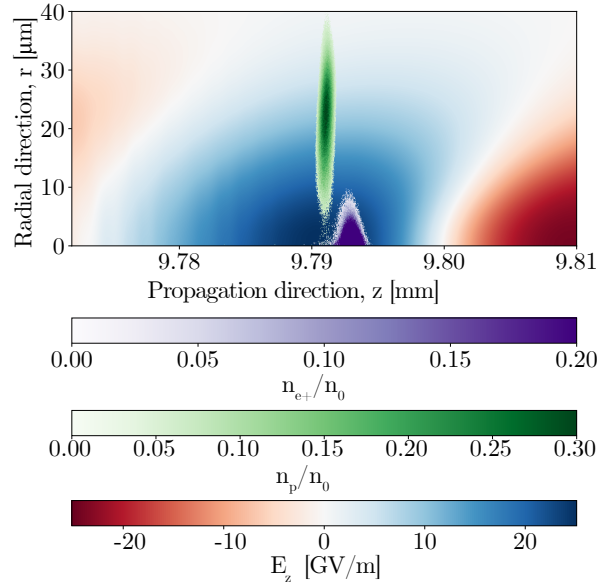


Figure 11. 2D plot of the primary electron (green color-map) and positron (purple) beam densities normalized to the peak plasma background density, overlapping the longitudinal plasma wakefield (red-blue).

efficiency $\eta_{e+} = 44.5\%$, the highest among the schemes considered in this paper. The evolution of the energy

Table 1. Initial ($z = 0$ mm) and final ($z = 10.20$ mm into the plasma) properties of the positrons within the AFP ($r < 20$ μm) region: charge Q , average beam energy, $\langle E \rangle$, RMS sizes $\sigma_{x,y,z}$, RMS divergence $\theta_{x,y}$, and normalized emittance, $\varepsilon_{x,y}$. Since the values in x and y are similar, the average result is presented for simplicity.

	Initial	Final
Q [pC]	5.7	4.2
$\langle E \rangle$ [GeV]	1.1	1.6
$\sigma_{x,y}$ [μm]	5.59	3.48
σ_z [μm]	0.47	0.50
$\theta_{x,y}$ [mrad]	10.1	3.4
$\varepsilon_{x,y}$ [μm]	32.1	20.7

distribution of the positrons is shown Fig. 12. The parameters of the positrons in the AFP ($r < 20$ μm) are summarized in Table 1, where the initial ($z = 0$ mm) and final ($z = 10.20$ mm into the plasma) charge, average energy, RMS longitudinal and transverse sizes, divergence, and normalized emittance are given.

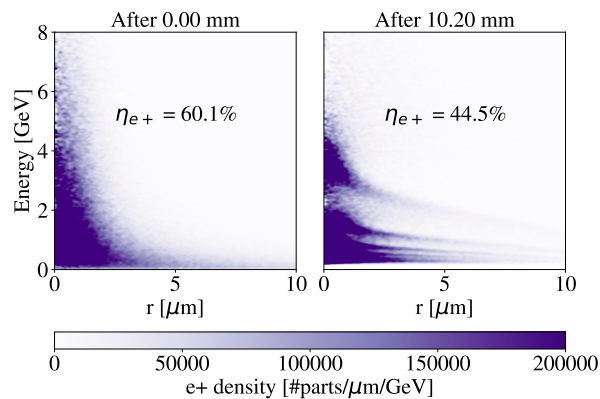


Figure 12. Initial ($z = 0$ mm, left) and final ($z = 10.20$ mm into the plasma, right) positron energy spectra along the radial direction.

6. Conclusions

In this paper we analyzed, by means of self-consistent simulations, the performance of different schemes to realize a compact, laser-plasma-based positron source. The schemes analyzed rely on a two-stage approach. The first stage is an LPA that generates a multi-GeV (primary) electron beam. Positrons are produced via bremsstrahlung when the primary beam interacts with a mm-scale high-Z foil. In the second stage some of the positrons are captured and accelerated in a plasma wave. These schemes employed laser-plasma configurations that were either demonstrated or expected to be demonstrated in the near future. We considered three positron source setups: (i) a single LPA-generated primary electron beam produces the

positrons in the foil, then both the primary beam and the positrons enter the second stage where the beam generates a wakefield that traps and accelerates some of the positrons. (ii) A train of two LPA-generated primary electron beams, which produce positrons in the foil, are sent into the plasma where the first beam excites the plasma wakefields that capture and accelerate some of the positrons produced by the trailing one on the foil. The positrons from the leading primary beam as well as the trailing primary beam and secondary electrons are defocused by this wakefield. (iii) A single LPA-produced primary electron beam creates positrons in the foil that are captured and accelerated in the quasi-linear wakefields generated by an independent laser pulse powering the plasma stage. Modeling different beam-foil configurations showed that there is a trade-off between increasing the number of created positrons and preserving the quality the primary electron beam and reducing the divergence and the transverse size of the positron distribution after the foil. These properties are mainly determined by the thickness and the material of the foil, and by the primary electron beam energy. Additionally, modeling showed that the positron trapping efficiencies for the three proposed source configurations is significantly different. More specifically, for scheme (i) the large divergence of both the primary electron beam and of the positrons after the foil, as well as the evolution of the primary beam in the second stage prevented most positrons from falling within the AFP region, and so less than 1% of positron were captured. The two beam scheme (ii) allowed for approximately 11% of the trailing positrons to be captured. Finally, the scheme (iii) demonstrated, potentially, the greatest capture efficiency, with 44% of the initially produced positrons captured in the second stage. We point out that the performance quoted for scheme (iii) should be consider an upper limit. Realistic performance will need to take into consideration a scheme to in-couple the laser pulse and the positrons into the plasma stage. One possible solution is proposed in Ref. [47], where the authors discuss a scheme that employs a plasma mirror.

Our results emphasize the need for taking into account multi-dimensional effects and coupling between the stages that create, capture, and accelerate positrons when considering the design of future plasma-based positron sources suitable for collider applications.

7. Acknowledgments

This work was supported by LDRD funding from LBNL provided by the Director, and the U.S. DOE Office of Science Offices of HEP under Contract No. DE-AC02-05CH11231 and by the Exascale Computing

Project (17-SC-20-SC), a collaborative effort of the Office of Science, US DOE and the National Nuclear Security Administration. This research used resources of the Oak Ridge Leadership Computing Facility at the Oak Ridge National Laboratory, which is supported by the Office of Science of the U.S. Department of Energy under Contract No. DE-AC05-00OR22725. This research used resources of the National Energy Research Scientific Computing Center (NERSC), a U.S. Department of Energy Office of Science User Facility located at Lawrence Berkeley National Laboratory, operated under Contract No. DE-AC02-05CH11231 using NERSC award HEP-ERCAP0023685. The input files, run scripts, and analysis scripts are available upon request, in future it is planned to create a persistent data archive at zenodo.org.

Appendix: Details on the GPos code

The code processed the trajectories and interactions of each of the primary electrons until they lost all their energy or hit the end of the *world* using the physics class `QGSP_BERT`, which models the physics of bremsstrahlung and pair production. Only the data from particles that did not leave the *world* transversely, nor had energy as well as longitudinal momentum below the minimum cutoffs of 5 MeV and 5 MeV/c, respectively (chosen such that positrons were relativistic, but slow enough to fall behind the primary beam after cm-long drifts), nor had distances greater than 4.0RMS beam sizes from the beam centroid for the spatial and momentum distributions in all directions (i.e., that were not outliers), was stored and processed. Particles were propagated backwards ballistically by a few μm to reach the same (minimum) final run time. The particles could also be transported ballistically during a vacuum drift encompassing a thin lens focusing the positrons, in the code. The results, with or without the drift and lens, including the physical process by which particles were created, were stored in `OPENPMD` (`OPENPMD-API` version 0.12.0) files-compatible with `WARPX` input format (release version 21.05). The `GPOS` simulations discussed here typically run on 1 node (or up to 25 nodes, when using thicker foils), resulting in a total of 20 (or 100) CPU cores on the NERSC computer cluster Cori, during less than 8 (or 30) minutes.

8. Bibliography

- [1] Shiltsev V and Zimmermann F 2021 *Rev. Mod. Phys.* **93**(1) 015006 URL <https://link.aps.org/doi/10.1103/RevModPhys.93.015006>
- [2] Tajima T and Dawson J M 1979 *Phys. Rev. Lett.* **43**(4) 267–270 URL <https://link.aps.org/doi/10.1103/PhysRevLett.43.267>
- [3] Esarey E, Schroeder C B and Leemans W P 2009 *Rev. Mod. Phys.* **81**(3) 1229–1285 URL <https://link.aps.org/doi/10.1103/RevModPhys.81.1229>
- [4] Joshi C, Corde S and Mori W B 2020 *Physics of Plasmas* **27** 070602 (*Preprint* <https://doi.org/10.1063/5.0004039>) URL <https://doi.org/10.1063/5.0004039>
- [5] National Academies of Sciences, Engineering, and Medicine 2021 *Plasma Science: Enabling Technology, Sustainability, Security, and Exploration* (Washington, DC: The National Academies Press) ISBN 978-0-309-67760-8
- [6] Caldwell A, Chappell J, Crivelli P, Depero E, Gall J, Gninenko S, Gschwendtner E, Hartin A, Keeble F, Osborne J, Pardons A, Petrenko A, Scaachi A and Wing M 2018 Particle physics applications of the awake acceleration scheme (*Preprint* 1812.11164)
- [7] Hidding B, Hooker S, Jamieson S, Muratori B, Murphy C, Najmudin Z, Pattahil R, Sarri G, Streeter M, Welsch C, Wing M and Xia G 2019 Plasma wakefield accelerator research 2019 - 2040: a community-driven UK roadmap compiled by the plasma wakefield accelerator steering committee (PWASC) Tech. rep. Plasma Wakefield Accelerator Steering Committee (PWASC)
- [8] Gonsalves A J, Nakamura K, Daniels J, Benedetti C, Pieronek C, de Raadt T C H, Steinke S, Bin J H, Bulanov S S, van Tilborg J, Geddes C G R, Schroeder C B, Tóth C, Esarey E, Swanson K, Fan-Chiang L, Bagdasarov G, Bobrova N, Gasilov V, Korn G, Sasorov P and Leemans W P 2019 *Phys. Rev. Lett.* **122**(8) 084801 URL <https://link.aps.org/doi/10.1103/PhysRevLett.122.084801>
- [9] Litos M, Adli E, An W, Clarke C I, Clayton C E, Corde S, Delahaye J P, England R J, Fisher A S, Frederico J, Gessner S, Green S Z, Hogan M J, Joshi C, Lu W, Marsh K A, Mori W B, Muggli P, Vafaei-Najafabadi N, Walz D, White G, Wu Z, Yakimenko V and Yocky G 2014 *Nature* **515** 92–95 ISSN 1476-4687 URL <https://doi.org/10.1038/nature13882>
- [10] Lindström C A 2021 *Phys. Rev. Accel. Beams* **24**(1) 014801 URL <https://link.aps.org/doi/10.1103/PhysRevAccelBeams.24.014801>
- [11] Corde S, Adli E, Allen J M, An W, Clarke C I, Clayton C E, Delahaye J P, Frederico J, Gessner S, Green S Z, Hogan M J, Joshi C, Lipkowitz N, Litos M, Lu W, Marsh K A, Mori W B, Schmeltz M, Vafaei-Najafabadi N, Walz D, Yakimenko V and Yocky G 2015 *Nature* **524** 442–445 ISSN 1476-4687 URL <https://doi.org/10.1038/nature14890>
- [12] Gessner S, Adli E, Allen J M, An W, Clarke C I, Clayton C E, Corde S, Delahaye J P, Frederico J, Green S Z, Hast C, Hogan M J, Joshi C, Lindström C A, Lipkowitz N, Litos M, Lu W, Marsh K A, Mori W B, O’Shea B, Vafaei-Najafabadi N, Walz D, Yakimenko V and Yocky G 2016 *Nature Communications* **7** 11785 ISSN 2041-1723 URL <https://doi.org/10.1038/ncomms11785>
- [13] Seimiya Y, Kuriki M, Takahashi T, Omori T, Okugi T, Satoh M, Urakawa J and Kashiwagi S 2015 *Progress of Theoretical and Experimental Physics* **2015** ISSN 2050-3911 103G01 (*Preprint* <https://academic.oup.com/ptep/article-pdf/2015/10/103G01/8085531/ptv136.pdf>) URL <https://doi.org/10.1093/ptep/ptv136>
- [14] Bambade P *et al.* 2019 The international linear collider a global project (*Preprint* hep-ex/1903.01629)
- [15] Musumeci P, Boffo C, Bulanov S S, Chaikovska I, Golfe A F, Gessner S, Grames J, Hessami R, Ivanyushenkov Y, Lankford A, Loisch G, Moortgat-Pick G, Nagaitsev S, Riemann S, Sievers P, Tenholt C and Yokoya K 2022 Positron Sources for Future High Energy Physics Colliders arXiv:2204.13245 [physics] URL <http://arxiv.org/abs/2204.13245>
- [16] Benedetti C, Bulanov S S, Esarey E, Geddes C G R,

- Gonsalves A J, Huebl A, Lehe R, Nakamura K, Schroeder C B, Terzani D, van Tilborg J, Turner M, Vay J L, Zhou T, Albert F, Bromage J, Campbell E M, Froula D H, Palastro J P, Zuegel J, Bruhwiler D, Cook N M, Cros B, Downer M C, Fuchs M, Shadwick B A, Gessner S J, Hogan M J, Hooker S M, Jing C, Krushelnick K, Thomas A G R, Leemans W P, Maier A R, Osterhoff J, Poder K, Thevenet M, Joshi C, Mori W B, Milchberg H M, Palmer M, Power J G and Vafaei-Najafabadi N 2022 Linear colliders based on laser-plasma accelerators arXiv:2203.08366 [physics] URL <http://arxiv.org/abs/2203.08366>
- [17] Wang X, Ischebeck R, Muggli P, Katsouleas T, Joshi C, Mori W B and Hogan M J 2008 *Phys. Rev. Lett.* **101**(12) 124801 URL <https://link.aps.org/doi/10.1103/PhysRevLett.101.124801>
- [18] Wang X, Muggli P, Katsouleas T, Joshi C, Mori W B, Ischebeck R and Hogan M J 2009 *Phys. Rev. ST Accel. Beams* **12**(5) 051303 URL <https://link.aps.org/doi/10.1103/PhysRevSTAB.12.051303>
- [19] Vieira J and Mendonça J T 2014 *Phys. Rev. Lett.* **112**(21) 215001 URL <https://link.aps.org/doi/10.1103/PhysRevLett.112.215001>
- [20] Amorim L D, Vieira J, Fonseca R A and Silva L O 2016 *AIP Conference Proceedings* **1777** 070001 (Preprint <https://aip.scitation.org/doi/pdf/10.1063/1.4965644>) URL <https://aip.scitation.org/doi/abs/10.1063/1.4965644>
- [21] Williams G J, Barnak D, Fiksel G, Hazi A, Kerr S, Krauland C, Link A, Manuel M J E, Nagel S R, Park J, Peebles J, Pollock B B, Beg F N, Betti R and Chen H 2016 *Physics of Plasmas* **23** 123109 (Preprint <https://doi.org/10.1063/1.4971235>) URL <https://doi.org/10.1063/1.4971235>
- [22] Joshi C, Adli E, An W, Clayton C E, Corde S, Gessner S, Hogan M J, Litos M, Lu W, Marsh K A, Mori W B, Vafaei-Najafabadi N, O'shea B, Xu X, White G and Yakimenko V 2018 *Plasma Phys. Control. Fusion* **60** 034001 URL <https://doi.org/10.1088/1361-6587/aaa2e3>
- [23] Sahai A A 2018 *Phys. Rev. Accel. Beams* **21**(8) 081301 URL <https://link.aps.org/doi/10.1103/PhysRevAccelBeams.21.081301>
- [24] Fujii H, Marsh K A, An W, Corde S, Hogan M J, Yakimenko V and Joshi C 2019 *Phys. Rev. ST Accel. Beams* **22**(9) 091301 URL <https://link.aps.org/doi/10.1103/PhysRevAccelBeams.22.091301>
- [25] Xu Z Y, Xiao C F, Lu H Y, Hu R H, Yu J Q, Gong Z, Shou Y R, Liu J X, Xie C Z, Chen S Y, Lu H G, Xu T Q, Li R X, Hafz N, Li S, Najmudin Z, Rajeev P P, Neely D and Yan X Q 2020 *Phys. Rev. Accel. Beams* **23**(9) 091301 URL <https://link.aps.org/doi/10.1103/PhysRevAccelBeams.23.091301>
- [26] Diederichs S, Benedetti C, Esarey E, Osterhoff J and Schroeder C B 2020 *Phys. Rev. Accel. Beams* **23**(12) 121301 URL <https://link.aps.org/doi/10.1103/PhysRevAccelBeams.23.121301>
- [27] Xu Z, Yi L, Shen B, Xu J, Ji L, Xu T, Zhang L, Li S and Xu Z 2020 *Communications Physics* **3** 191 URL <https://doi.org/10.1038/s42005-020-00471-6>
- [28] Zhou S, Hua J, An W, Mori W B, Joshi C, Gao J and Lu W 2021 *Phys. Rev. Lett.* **127**(17) 174801 URL <https://link.aps.org/doi/10.1103/PhysRevLett.127.174801>
- [29] Gonoskov A, Blackburn T G, Marklund M and Bulanov S S 2022 *Reviews of Modern Physics* **94** 045001 publisher: American Physical Society URL <https://link.aps.org/doi/10.1103/RevModPhys.94.045001>
- [30] Warwick J, Alejo A, Dzelzainis T, Schumaker W, Doria D, Romagnani L, Poder K, Cole J, Yeung M, Krushelnick K, Mangles S, Najmudin Z, Samarin G, Symes D, Thomas A, Borghesi M and Sarri G 2018 *Nuclear Instruments and Methods in Physics Research Section A: Accelerators, Spectrometers, Detectors and Associated Equipment* **909** 95–101 ISSN 0168-9002 3rd European Advanced Accelerator Concepts workshop (EAAC2017) URL <https://www.sciencedirect.com/science/article/pii/S0168900218302080>
- [31] Alejo A, Samarin G M, Warwick J, McCluskey C, Cantono G, Ceccotti T, Dufrénoy S D, Monot P and Sarri G 2020 *Plasma Physics and Controlled Fusion* **62** 055013 URL <https://doi.org/10.1088/1361-6587/ab7e81>
- [32] van Tilborg J, Steinke S, Geddes C G R, Matlis N H, Shaw B H, Gonsalves A J, Huijts J V, Nakamura K, Daniels J, Schroeder C B, Benedetti C, Esarey E, Bulanov S S, Bobrova N A, Sasorov P V and Leemans W P 2015 *Phys. Rev. Lett.* **115**(18) 184802 URL <https://link.aps.org/doi/10.1103/PhysRevLett.115.184802>
- [33] van Tilborg J, Barber S K, Tsai H E, Swanson K K, Steinke S, Geddes C G R, Gonsalves A J, Schroeder C B, Esarey E, Bulanov S S, Bobrova N A, Sasorov P V and Leemans W P 2017 *Phys. Rev. Accel. Beams* **20**(3) 032803 URL <https://link.aps.org/doi/10.1103/PhysRevAccelBeams.20.032803>
- [34] Pompili R, Anania M P, Bellaveglia M, Biagioni A, Bini S, Bisesto F, Brentegani E, Cardelli F, Castorina G, Chiadroni E, Cianchi A, Coiro O, Costa G, Croia M, Di Giovenale D, Ferrario M, Filippi F, Giribono A, Lollo V, Marocchino A, Marongiu M, Martinelli V, Mostacci A, Pellegrini D, Piersanti L, Di Pirro G, Romeo S, Rossi A R, Scifo J, Shpakov V, Stella A, Vaccarezza C, Villa F and Zigler A 2018 *Phys. Rev. Lett.* **121**(17) 174801 URL <https://link.aps.org/doi/10.1103/PhysRevLett.121.174801>
- [35] Amorim L D, Bulanov S S, Benedetti C, Huebl A, Schroeder C and Vay J L 2021 Gpos: an easy-to-use geant4-based open-source tool for modeling positron generation in solid-targets URL <https://github.com/LDAmorim/Gpos>
- [36] Agostinelli S, Allison J, Amako K a, Apostolakis J, Araujo H, Arce P, Asai M, Axen D, Banerjee S, Barrand G and others 2003 *Nuclear instruments and methods in physics research section A: Accelerators, Spectrometers, Detectors and Associated Equipment* **506** 250–303 publisher: Elsevier
- [37] Allison J, Amako K, Apostolakis J, Araujo H, Arce Dubois P, Asai M, Barrand G, Capra R, Chauvie S, Chytráček R, Cirrone G, Cooperman G, Cosmo G, Cuttner G, Daquino G, Donszelmann M, DRESSL M, Folger G, Foppiano F, Generowicz J, Grichine V, Guatelli S, Gumplinger P, Heikkinen A, Hrivnacova I, Howard A, Incerti S, Ivanchenko V, Johnson T, Jones F, Koi T, Koukoulis R, Kossov M, Kurashige H, Lara V, Larsson S, Lei F, Link O, Longo F, Maire M, Mantero A, Mascialino B, McLaren I, Mendez Lorenzo P, Minamimoto K, Murakami K, Nieminen P, Pandola L, Parlati S, Peralta L, Perl J, Pfeiffer A, Pia M, Ribon A, Rodrigues P, Russo G, Sadilov S, Santin G, Sasaki T, Smith D, Starkov N, Tanaka S, Tcherniaev E, Tome B, Trindade A, Truscott P, Urban L, Verderi M, Walkden A, Wellisch J, Williams D, Wright D and Yoshida H 2006 *IEEE Transactions on Nuclear Science* **53** 270–278
- [38] Allison J, Amako K, Apostolakis J, Arce P, Asai M, Aso T, Bagli E, Bagulya A, Banerjee S, Barrand G and others 2016 *Nuclear instruments and methods in physics research section A: Accelerators, Spectrometers, Detectors and Associated Equipment* **835** 186–225 publisher: Elsevier
- [39] Benedetti C, Schroeder C, Mehrling T, Djordjevic B, Bulanov S, Geddes C, Esarey E and Leemans W 2018 Inf&rno modeling of 10 gev-class electron beams from a laser-plasma accelerator driven by the bella laser 2018

IEEE Advanced Accelerator Concepts Workshop (AAC)
pp 1–5

- [40] Chao A W, Mess K H and others 2013 *Handbook of accelerator physics and engineering* (World scientific)
- [41] Vay J L, Huebl A, Almgren A, Amorim L D, Bell J, Fedeli L, Ge L, Gott K, Grote D P, Hogan M, Jambunathan R, Lehe R, Myers A, Ng C, Rowan M, Shapoval O, Thévenet M, Vincenti H, Yang E, Zaim N, Zhang W, Zhao Y and Zoni E 2021 *Phys. Plasmas* **28** 023105 (Preprint <https://doi.org/10.1063/5.0028512>) URL <https://doi.org/10.1063/5.0028512>
- [42] Fedeli L, Huebl A, Boillod-Cerneux F, Clark T, Gott K, Hillairet C, Jaure S, Leblanc A, Lehe R, Myers A, Piechurski C, Sato M, Zaim N, Zhang W, Vay J L and Vincenti H 2022 Pushing the frontier in the design of laser-based electron accelerators with groundbreaking mesh-refined particle-in-cell simulations on exascale-class supercomputers *SC22: International Conference for High Performance Computing, Networking, Storage and Analysis* (IEEE)
- [43] Lu W, Huang C, Zhou M M, Mori W B and Katsouleas T 2005 *Phys. Plasmas* **12** 063101 (Preprint <https://doi.org/10.1063/1.1905587>) URL <https://doi.org/10.1063/1.1905587>
- [44] Chen M, Sheng Z M, Ma Y Y and Zhang J 2006 *Journal of Applied Physics* **99** 056109 (Preprint <https://doi.org/10.1063/1.2179194>) URL <https://doi.org/10.1063/1.2179194>
- [45] Pak A, Marsh K A, Martins S F, Lu W, Mori W B and Joshi C 2010 *Phys. Rev. Lett.* **104**(2) 025003 URL <https://link.aps.org/doi/10.1103/PhysRevLett.104.025003>
- [46] McGuffey C, Thomas A G R, Schumaker W, Matsuoka T, Chvykov V, Dollar F J, Kalintchenko G, Yanovsky V, Maksimchuk A, Krushelnick K, Bychenkov V Y, Glazyrin I V and Karpeev A V 2010 *Phys. Rev. Lett.* **104**(2) 025004 URL <https://link.aps.org/doi/10.1103/PhysRevLett.104.025004>
- [47] Terzani D, Benedetti C, Bulanov S S, Schroeder C B and Esarey E 2023 *submitted*